

# Specific Production of Atomic Oxygen near Barrier Surface in Pin-to-sphere Positive Pulsed Discharge in Sub-atmospheric Pressure Pure Oxygen

Y. Nakagawa, J. Ogaki and F. Tochikubo

Department of Electrical Engineering and Computer Science, Tokyo Metropolitan University, Tokyo, Japan

**Abstract:** We investigated the behaviour of atomic oxygen in pin-to-sphere pulsed barrier discharge in sub-atmospheric pressure pure O<sub>2</sub>, where the radical lifetime may be extended without decreasing their production amount. The specific production of atomic oxygen near the barrier surface was observed, whereas that at metal-to-metal discharge did not show biased distribution near the cathode. The specific O production near the barrier can arise from the enhanced density or expanded O-productive area with relatively low-energy electrons.

**Keywords:** sub-atmospheric pressure discharge, atomic oxygen, laser spectroscopy.

## 1. Introduction

In the plasma chemical applications including surface modification, medical treatment, and environmental improvement, radical flux to the target is one of the most important parameters which predominates the chemical reactions. Atmospheric-pressure plasma can produce high-density radicals, but the radicals have a relatively short lifetime due to frequent collisions between radicals and background gas. Sub-atmospheric pressure plasma, which is the plasma at the pressure slightly decreased from atmosphere (namely 0.1–0.9 atm), is considered to have capability to extend radical lifetime without decreasing the radical amount[1], leading to improved radical flux. However, the radical behaviour in sub-atmospheric pressure is not clarified in detail.

In this study, we measured the behaviour of atomic oxygen in sub-atmospheric pressure discharge. Atomic oxygen is one of the most popular oxidative radicals produced in the air discharge. Pressure dependence and spatial distribution of atomic oxygen under the pin-to-sphere pulsed discharge were investigated by laser spectroscopy.

## 2. Experiments

### 2.1. TALIF for atomic oxygen

Ground state atomic oxygen O(2p<sup>4</sup> 3P) was measured using two-photon absorption laser-induced fluorescence (TALIF) technique[2,3]. Figure 1 represents the energy levels related to TALIF of O(2p<sup>4</sup> 3P). A 225.6 nm laser excites O(2p<sup>4</sup> 3P) to O(2p<sup>3</sup>3p 3P), and an 844.6 nm fluorescence is observed as a signal. The TALIF signal  $S_F$

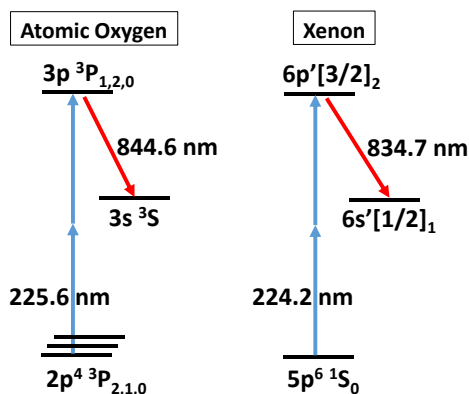


Fig. 1. Energy diagram of TALIF for O and Xe.

is integrated over time, volume, and wavelength, and expressed in terms of the O(2p<sup>4</sup> 3P) density  $n_O$  and laser energy  $E_L$  as below:

$$S_F = c_F \frac{A_F}{\Gamma} n_O \sigma^{(2)} E_L^2, \quad (1)$$

where  $c_F$ ,  $A_F$ ,  $\Gamma$ , and  $\sigma^{(2)}$  are the experimental constant, emission coefficient of the observed fluorescence, total deexcitation rate of the excited state, and two-photon absorption cross section, respectively. Hereafter, the word ‘atomic oxygen’ refers to the ground state O(2p<sup>4</sup> 3P). The absolute density of atomic oxygen was calibrated by TALIF of Xe [4,5].

### 2.2. Experimental settings

Experimental system for TALIF measurements is represented in Fig. 2. An Nd:YAG (355 nm)-pumped pulsed dye laser (Scanmate 2C400, Lambda Physik) generated a 451 nm beam, which was converted to a 226 nm beam by second-harmonic generation. The 226 nm laser was introduced to the observed area, and the beam was vertically focused into a sheet shape on the discharge area by a cylindrical lens with 200 mm focal length. Fluorescence was detected by a photomultiplier tube (R13456, Hamamatsu), and the stray light of the excitation laser was blocked by optical band-pass and high-pass filters (FF01-840/12-25 and FF01-300/LP-25, Semrock). The fluorescence from the excited O was collected by collimating and focusing lenses positioned perpendicularly to both the laser axis and quartz tube axis. The horizontal width of the laser was 5 mm, and the estimated laser beam waist size in the vertical direction was approximately 5–10 μm. The time-averaged laser energy was measured by a laser power meter (PowerMAX-USB PM3, Coherent). An

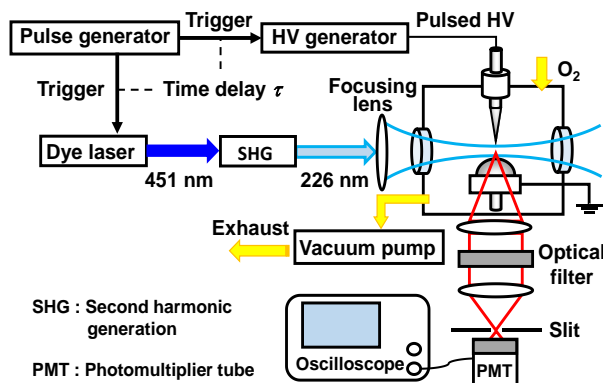


Fig. 2. Schematic of experimental system.

excitation laser pulse was delayed from a discharge pulse using a delay generator (DG535, Stanford Research Systems), and the time evolution of the TALIF signal after a discharge pulse was measured by changing the time delay  $\tau$ . The experimental TALIF signals and laser energies were averaged over 512 shots at each measurement condition. The TALIF signal was compensated using the signals at off-resonant of TALIF excitation and without laser irradiation, thereby eliminating the parasitic signals of discharge emission and laser scattering.

### 2.3. Discharge configurations

Pure O<sub>2</sub> gas was supplied to the reactor with dimensions of  $15 \times 15 \times 20 \text{ cm}^3$ , at a flow rate of 2.0 L/min. The pressure inside the reactor was reduced by a diaphragm pump (DTC-60, Ulvac) and adjusted to be 20–95 kPa using a needle valve. A 0.5-mm-diameter stainless needle and a 15-mm-diameter stainless ball were positioned oppositely in the center of the reactor. In dielectric-barrier discharge (DBD) configuration, the stainless ball was covered by a borosilicate glass hemisphere with a thickness of 0.4 mm and a diameter of 20 mm. The gap length from the needle tip to the top of the glass hemisphere was adjusted to be 1.1 mm. A pulsed high voltage (HV) was applied to the needle electrode to trigger the positive pulsed discharge at the rate of 10 pps. The peak value of the pulsed voltage was adjusted so that the discharge energy remained constant with the variation of the pressure.

## 3. Results and Discussion

### 3.1. Discharge characteristics

Figures 3 and 4 represent the voltage-current waveforms and discharge emission image captured by ICCD camera

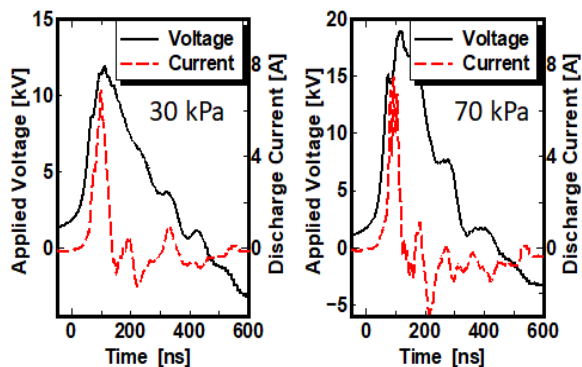


Fig. 3. Voltage-current waveforms at 30/70 kPa DBD.

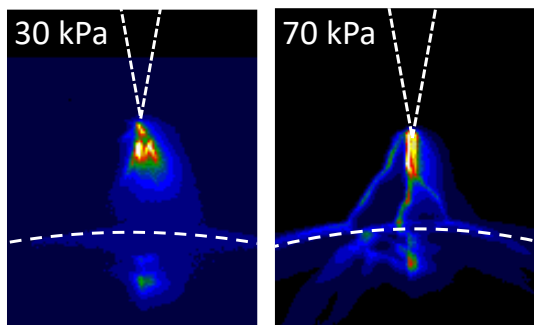


Fig. 4. Discharge emission images at 30/70 kPa DBD.

(iStar DH734I, Andor) at 30/70 kPa in DBD configuration. The exposure gate of ICCD was 100 ns for each images to include whole discharge emission. The current duration was extended by decreasing pressure. The discharge form was filamentary streamers at the pressure above 50 kPa, whereas the discharge was relatively uniform and distributed near the anode at the pressure below 30 kPa.

### 3.2. Pressure dependence of O behaviour in DBD

Temporal profiles of atomic oxygen at 20–95 kPa near the anode (0.1 mm from anode) or near the cathode (0.1 mm from cathode) are represented in Figs. 5 and 6, respectively. The discharge energy was adjusted to be 3 mJ. Here the atomic oxygen density is the value averaged over the observed volume ( $5 \times 6.25 \times 0.005\text{--}0.01 \text{ mm}^3$ ), not the local density in the plasma. Figures 5 and 6 exhibit the extension of the atomic-oxygen lifetime by decreasing pressure regardless of the observed position.

Figure 7 represents the spatial distributions of atomic oxygen just after the discharge ( $\tau = 3 \mu\text{s}$ ). The discharge energy was adjusted to be approximately 2.7 mJ. The atomic oxygen had a relatively flat profile at atmospheric pressure (95 kPa), whereas the atomic oxygen at sub-atmospheric pressure (20–70 kPa) exhibited localized distributions near the cathode.

According to the spatial distribution at  $\tau = 3 \mu\text{s}$ , the pressure dependence of atomic oxygen produced by discharge is represented in Fig. 8. Figure 8 exhibits the features below:

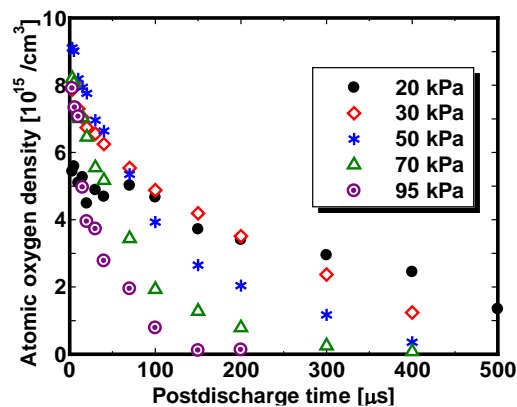


Fig. 5. Time evolution of O atom near the anode.

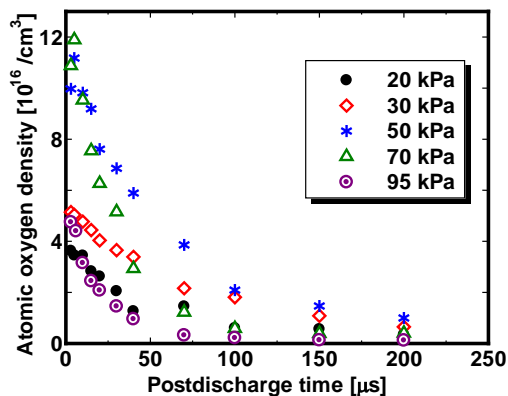


Fig. 6. Time evolution of O atom near the cathode.

Table 1. Main reactions related to decay of atomic oxygen.

Reaction	Rate coefficient at 420 K	Half life period at 50 kPa, 420 K	
		at $n_p = 7 \times 10^{16} \text{ cm}^{-3}$	at $n_p = 7 \times 10^{17} \text{ cm}^{-3}$
R1 O + O + M $\rightarrow$ O <sub>2</sub> + M	$3.8 \times 10^{-34} \text{ [cm}^6/\text{s]}$	1.3 ms	190 $\mu\text{s}$
R2 O + O <sub>2</sub> + M $\rightarrow$ O <sub>3</sub> + M	$1.2 \times 10^{-34} \text{ [cm}^6/\text{s]}$	65 $\mu\text{s}$	65 $\mu\text{s}$

i) at sub-atmospheric pressure, the O production amount near the cathode is much larger than near the anode,  
 ii) the O density near the cathode has a local maximum near 50 kPa.

The feature ii) is quite important, because it means that the sub-atmospheric O<sub>2</sub> discharge can extend the lifetime of atomic oxygen with improvement of atomic oxygen production. The relative yield  $\Phi_O$  of atomic oxygen near the electrode can be evaluated by

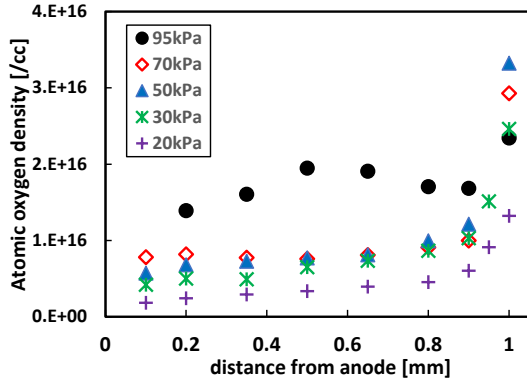
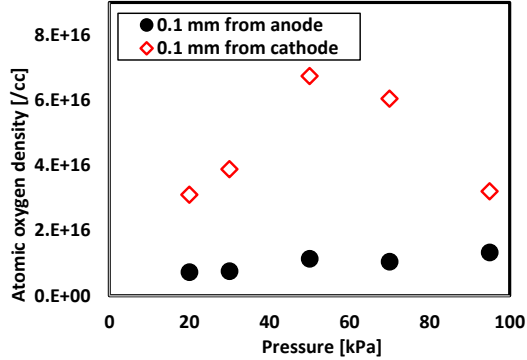

 Fig. 7. Spatial distribution of O atom at  $\tau = 3 \mu\text{s}$ .


Fig. 8. Pressure dependence of O density.

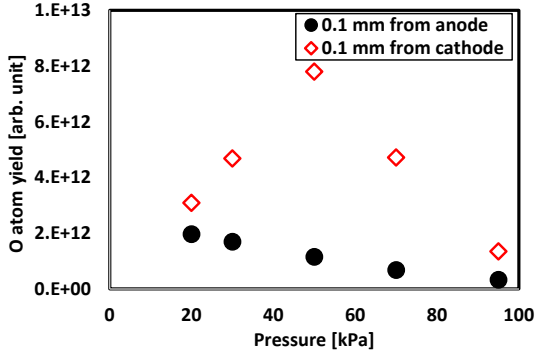


Fig. 9. Discharge emission images at 30/70 kPa DBD.

$$\Phi_O \propto \int [O] dt. \quad (2)$$

The relative atomic oxygen yield against the pressure is represented in Fig. 9. The relative O yield near the cathode had a large local maximum at 50 kPa as a result of O-density improvement and lifetime extension. The O yield at 50 kPa was approximately 6 times of that at atmospheric pressure (95 kPa), indicating an enhancement of chemical reactions involving atomic oxygen. The atomic oxygen yield near the anode was also improved by decreasing pressure, because the lifetime of atomic oxygen was extended without substantial suppression of O density.

### 3.3. Reason for O density localization near cathode

The O density averaged over the observed volume  $n_O$  can be expressed by the local O density in the plasma,  $n_p$ , and the O-productive volume in the plasma,  $V_p$ , as below:

$$n_O = n_p \times V_p. \quad (3)$$

Therefore, reason for the specific increase in O production near the cathode can be attributed to two factors:

- The local O density  $n_p$  in the plasma region increased.
- The O-productive area  $V_p$  of the plasma stretched.

To evaluate the local O density, the decay rate of atomic oxygen at 50 kPa is plotted in Fig. 10. The O density in Fig. 10 is normalized by the value at  $\tau = 3 \mu\text{s}$ . The main reactions related to O decay is listed in Table 1, the self recombination of atomic oxygen (R1) and the ozone production reaction (R2). Here the half life value of recombination R1 depends on the initial value of  $n_p$ , whereas that of R2 is independent of  $n_p$ . Therefore, we can evaluate the local density by the decay rate. According to Fig. 10, the decay rate near the cathode was faster than the other position. This result indicate that the local O density near the cathode was higher than those near the cathode or at center of the discharge gap. However, quantitative estimation of local O density near the anode is difficult, because the decay rate by R2 is significantly fast compared

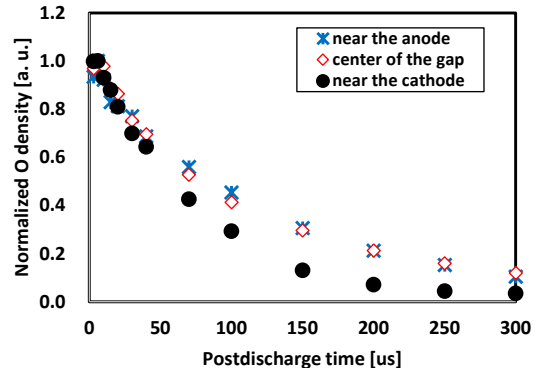


Fig. 10. Decay of normalized O density at 50 kPa.

with that of R1 at considerable gas temperature (see Table 1), leading to O-density independent decay rate.

As for the effect of expansion of O-productive area  $V_P$ , the discharge images at sub-atmospheric pressure (Fig. 4) do not exhibit any strong discharge emission along the discharge surface. Therefore, we cannot recognize the ionization wave propagating along the barrier surface (so-called 'surface discharge'). However, the ionization threshold of  $O_2$  is approximately 12 eV, whereas the dissociation threshold for O production is approximately 5.1 eV. Thus, the O-productive area may not coincide with the discharge emission. As a consequence, there remains both possibility of increase in  $n_P$  and expansion of  $V_P$  as the reason for specific O production near the cathode.

### 3.4. Comparison with metal-to-metal discharge

Spatial distribution of atomic oxygen was measured in a metal-to-metal electrode configuration to evaluate whether the specific O production near the cathode is a phenomenon unique to barrier discharges. The cathode was 15-mm-diameter stainless ball not covered with glass, and the discharge gap was adjusted to be 1.1 mm, the same gap length as barrier-discharge configuration. The pulsed voltage duration was shortened to be 35 ns to avoid spark discharges, thus the discharge energy was approximately 0.5 mJ, which was less than that in barrier discharges.

Figures 11 and 12 represent the spatial distributions of atomic oxygen at 30/70 kPa. The specific O production near the cathode was not observed at any pressure of 20, 30, 50, 70, or 95 kPa. Furthermore, the atomic oxygen exhibited fast decays near the anode, which indicates high

local O density near the anode. These features are different from those in the barrier-discharge configuration, therefore we can conclude that the specific O production near the cathode is a phenomenon unique to barrier discharge in sub-atmospheric pressure. Further investigation is required to identify the reason for this phenomenon.

### 4. Conclusion

We investigated the behaviour of atomic oxygen in pin-to-sphere pulsed barrier discharge in sub-atmospheric pressure pure  $O_2$ , where the radical lifetime may be extended without decreasing their production amount. The specific production of atomic oxygen near the barrier surface was observed, whereas that at metal-to-metal discharge did not show biased distribution near the cathode. The specific O production near the barrier can arise from the enhanced density or expanded O-productive area with relatively low-energy electrons.

### References

- [1] Y. Nakagawa *et al.*, *J. Appl. Phys.*, **131**, 113304 (2022).
- [2] K. Niemi *et al.*, *Plasma Sources Sci. Technol.*, **14**, 375 (2005)
- [3] A. V. Klochko *et al.*, *Plasma Sources Sci. Technol.*, **24**, 025010 (2015)
- [4] H. F. Dobeles, *et al.*, *Plasma Sources Sci. Technol.*, **14**, S31 (2005)
- [5] J. B. Schmidt *et al.*, *J. Phys. D: Appl. Phys.*, **50**, 015204 (2017)

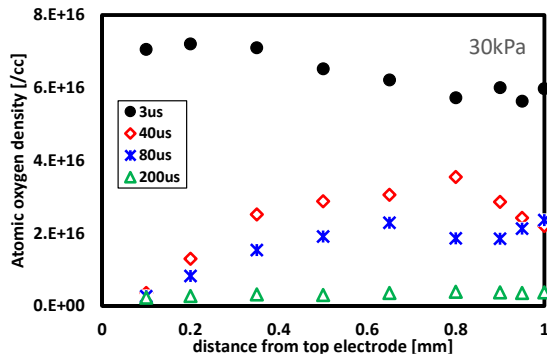


Fig. 11. Spatial distribution of O density at 30 kPa in the corona discharge with metal electrodes.

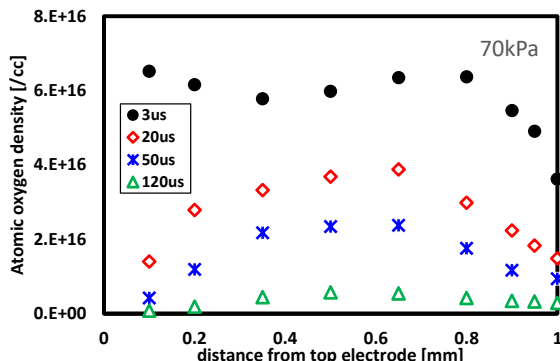


Fig. 12. Spatial distribution of O density at 70 kPa in the corona discharge with metal electrodes.